ADVANCED QUANTUM TECHNOLOGIES
www.advquantumtech.com

Magnetic Field Sensitivity Optimization of Negatively Charged Boron Vacancy Defects in hBN.

Benjamin Whitefield, Milos Toth, Igor Aharonovich, Jean-Philippe Tetienne, and Mehran Kianinia*

Optically active spin defects in hexagonal boron nitride (hBN) have recently emerged as compelling quantum sensors hosted by a two dimensional (2D) material. The photodynamics and sensitivity of spin defects are governed by their level structure and associated transition rates. These are, however, poorly understood for spin defects in hBN. Here, optical and microwave pump-probe measurements are used to characterize the relaxation dynamics of the negatively charged boron vacancy (V_B^-)—the most widely-studied spin defect in hBN. A 5-level model is used to deduce transition rates that give rise to spin-dependent V_B^- photoluminescence, and the lifetime of the V_B^- intersystem crossing metastable state. The obtained rates are used to simulate the magnetic field sensitivity of V_B^- defects and demonstrate high resolution imaging of the magnetic field generated by a single magnetic particle using optimal sensing parameters predicted by the model. The results reveal the rates that underpin V_B^- photodynamics, which is important for both a fundamental understanding of the V_B^- as a spin-photon interface and for achieving optimal sensitivity in quantum sensing applications.

1. Introduction

Quantum sensors have great potential for measuring a wide range of physical and chemical properties with unprecedented resolution and accuracy.[1–4] Among them, solid-state spin defects such as the nitrogen-vacancy center in diamond offer optical control and readout, room temperature operation, and remote sensing possibilities.[5–7] Recently, spin defects in hexagonal boron nitride (hBN) have gained interest due to the two dimensional (2D) layered nature of the host crystal with benefits of precise control over the dimensionality of the quantum sensor.[8–14] The negatively charged boron vacancy (V_B^-) defect has been used to detect temperature, electric current in 2D devices, strain and paramagnetic ions in liquids.[15–24] While these studies demonstrate the sensing capabilities of V_B^-, details of its spin-dependent photodynamics are yet to be studied in detail—both fundamentally and to optimize V_B^- sensing performance (e.g., by tuning excitation parameters).

The V_B^- is a spin-1 system with triplet ground and excited states. The zero-field splitting of the ground state is 3.47 GHz with a transverse splitting of 50–100 MHz at room temperature.[7,25–27] In the excited state, the zero field splitting is ≈2.1 GHz with a larger transverse splitting compared to the ground state.[28–31] Its photoluminescence (PL) intensity is spin-dependent due to a non-radiative pathway (intersystem crossing) through a metastable singlet state.[28,32,33] This gives rise to optically detected magnetic resonance (ODMR) contrast when the electron spin is manipulated by an external microwave field. Decay rates out of the excited state $m_s = 0$ and $m_s = \pm 1$ sublevels have been measured through fluorescence lifetime measurements to be ≈1 ns^{-1} and ≈2 ns^{-1}, respectively.[28] However, the photodynamics of V_B^- are also influenced critically by the contribution of the intersystem crossing to these decay rates, as well as by the transition rates from the metastable state to the ground state spin sublevels, which have not been measured to date.

In this work, we perform a photodynamics study of V_B^- ensembles and employ a simple 5-level transition rate model to explain spin-dependent relaxation of the V_B^- system. In particular, we use a combination of laser and microwave pulses to initialize and manipulate the V_B^- ground state electron spin state, and measure the time-resolved V_B^- PL intensity. We model the photodynamics using the 5-level model,[34–36] use it to deduce the V_B^- intersystem crossing rates, and map the magnetic field sensitivity dependency on microwave and laser excitation conditions. We conclude by measuring the magnetic field sensitivity of V_B^- at

B. Whitefield, M. Toth, I. Aharonovich, M. Kianinia
School of Mathematical and Physical Sciences
University of Technology Sydney
Ultimo, New South Wales 2007, Australia
E-mail: igor.aharonovich@uts.edu.au
B. Whitefield, M. Toth, I. Aharonovich, M. Kianinia
ARC Centre of Excellence for Transformative Meta-Optical Systems
Faculty of Science
University of Technology Sydney
Ultimo, New South Wales 2007, Australia
J.-P. Tetienne
School of Science
RMIT University
Melbourne, Victoria 3001, Australia

The ORCID identification number(s) for the author(s) of this article can be found under https://doi.org/10.1002/qute.202300118

DOI: 10.1002/qute.202300118

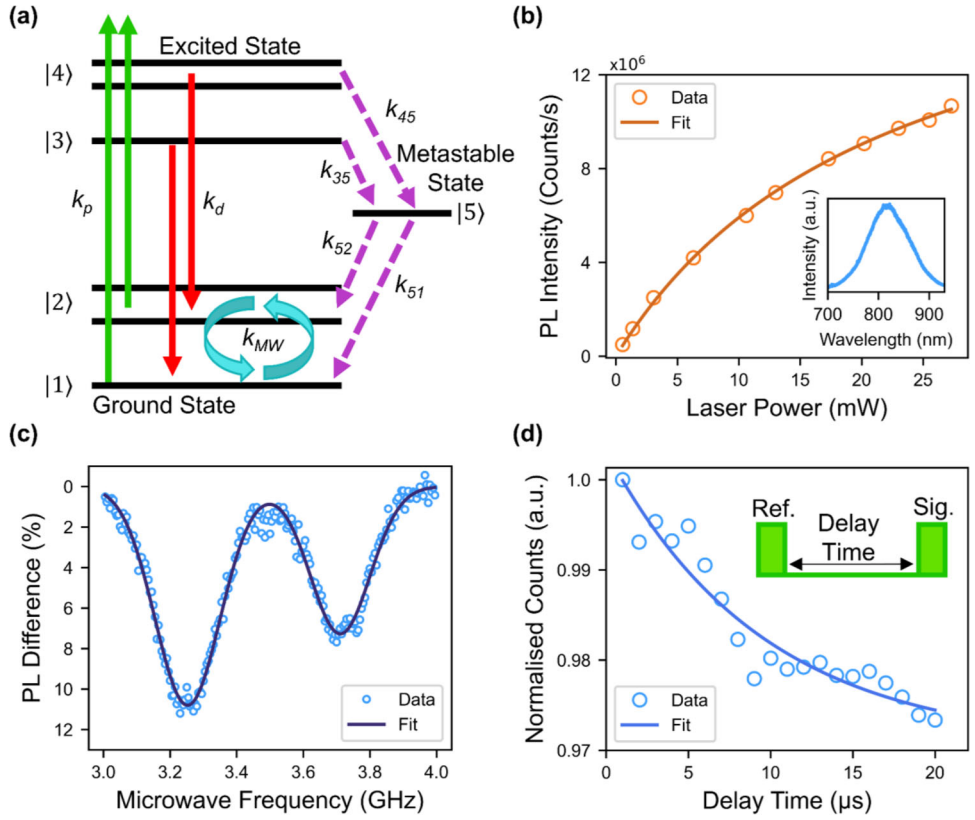

Figure 1. a) Simplified 5-level energy diagram of the V_B^- defect. The $m_s = +1$ and $m_s = -1$ spin states are combined into $|2\rangle$ and $|4\rangle$ for the ground and excited state, respectively. Arrows indicate various transitions between sublevels with $k_d = k_r + k_{nr}$ being the direct decay rate. b) PL saturation curve of the V_B^- ensemble used in this investigation. A PL saturation power of 22.5 ± 1.2 mW was deduced by fitting the data with $I = I_\infty \times P / (P + P_{sat})$. Inset: PL spectrum of the ensemble excited by a 532 nm laser. c) ODMR spectrum of the ensemble with two resonances corresponding to transitions from $m_s = 0$ to $m_s = -1$ and $m_s = +1$. The ODMR was recorded in the presence of an 8 mT external magnetic field. See Supporting Information for more details on ODMR measurements. d) Photoluminescence of the V_B^- ensemble versus delay time, normalized as signal/reference pulses which are shown schematically in the inset. The data was fit with an exponential and the T_1 was found to be 9.5 ± 2.8 μs.

various microwave and laser powers, and demonstrate high sensitivity magnetic imaging of a single magnetic particle.

2. Results and Discussions

The radiative and non-radiative transitions within the V_B^- energy structure occur at different rates that result in ODMR contrast. In the 5-level model, we combined the $m_s = +1$ and $m_s = -1$ spin states into a single spin state $|2\rangle$ for the electronic ground state, and spin state $|4\rangle$ for the excited state, as is illustrated in **Figure 1**a. This approximation is valid in the regime of low magnetic fields (<10 mT).[34] Off-resonant optical pumping by a 532 nm laser (k_p) excites electrons from the $|1\rangle$ and $|2\rangle$ states to $|3\rangle$ and $|4\rangle$, respectively, in a spin-conserving manner. k_d represents the direct decay rate from the excited to the ground state. It consists of both radiative and non-radiative components ($k_d = k_r + k_{nr}$). The direct decay k_d is considered to be spin-conserving (i.e., non-spin conserving decays from $|4\rangle$ to $|1\rangle$ and $|3\rangle$ to $|2\rangle$ are considered to be negligible). Non-radiative decay via the intersystem crossing is assumed to proceed through a single rate-limiting state $|5\rangle$, referred to as the metastable state, and the associated intersystem crossing rates are k_{35}, k_{45}, k_{51}, and k_{52}. k_{MW} denotes the rate of the spin flip transition $|1\rangle \rightarrow |2\rangle$ within the ground state, induced by an external resonant microwave field.

To generate an ensemble of V_B^- defects, an exfoliated hBN flake was irradiated with H^+ ions. The flake was then transferred onto a gold strip which acts as a microwave antenna for ODMR measurements (see Supporting Information for more details). A typical PL spectrum (related to the k_r transition) from the V_B^- centers excited by a 532 nm laser at room temperature is shown in the inset of Figure 1b. The PL emission was measured versus excitation power and fit with the equation $I = I_\infty \times P/(P + P_{sat})$, where I is PL intensity, I_∞ is PL intensity at saturation, P is excitation laser power, and P_{sat} is the laser power at saturation. The emission saturates at 22.5 ± 1.2 mW as is depicted in Figure 1b. Here on, we use the relative laser power, S, defined as the ratio of laser power to P_{sat} (i.e., $S = P / P_{sat}$). Spin Rabi measurements were also performed (Figure S1, Supporting Information) and used to represent microwave power as Rabi frequency (Ω_R) in radians per second, with a correspondence with the rate k_{MW} used in the 5-level model.

ODMR is achieved by cycling electrons from the $|1\rangle$ spin state to $|2\rangle$ with a resonant microwave while monitoring the PL emission. Electrons excited from $|2\rangle$ to $|4\rangle$ are more likely to decay via the intersystem crossing (i.e., $k_{45} > k_{35}$), which will result in

a reduced PL intensity and create ODMR contrast. In Figure 1c, a typical ODMR measurement is shown, where the external microwave was swept from 3 to 4 GHz and the difference in photon counts (ODMR contrast %) is plotted for each microwave frequency. In this measurement, an external magnetic field of 8 mT was applied to the sample which increases the gap between the $m_s = +1$ and -1 resonant frequencies through the Zeeman effect. The ODMR spectrum was acquired under continuous laser and microwave excitation (CW-ODMR), and the data are fit with a double inverse Gaussian curve. See the Supporting Information for further details on ODMR measurements and their analysis. The spin-lattice relaxation time (T_1) was measured, as is shown in Figure 1d where the employed pulse sequence is shown as an inset. The time between pulses was increased and the PL intensity from each pulse was normalized to the reference signal. The data is fit with an exponential and the T_1 relaxation time was found to be 9.5 ± 2.8 μs. In Figure 1d, as well as all future measurements that investigate a single spin transition, the transition $m_s = -1$ was selected for observation.

To build our understanding of optimal sensing parameters, we begin by examining the internal transition rates within the V_B^- energy structure. To achieve this, we first employ the 5-level model to globally fit a set of time-resolved PL traces when the system is polarized to three different states, which allows us to determine the previously unknown transition rates. We then use the same model and the inferred transition rates to predict the ODMR contrast at various laser and microwave powers, and compare to independent experimental data to assist in validating the model.

Figure 2a shows the three pulse sequences used to achieve these polarization conditions. The first laser pulse initializes the V_B^- into $m_s = 0$ state and the second pulse is used to record spin-dependent photoluminescence. In the first case, a 50 μs delay between the two pulses was used which is much longer than the spin-lattice relaxation time (T_1) of 9.5 ± 2.8 μs. Hence, the PL is from V_B^- in an unpolarized spin state, that is, the thermal mixture of $|1\rangle$ and $|2\rangle$ shown in Figure 2b. To create the P_A state, where the electrons are primarily (in the ideal case) polarized in $|1\rangle$, the delay time is reduced to 2 μs which is much shorter than T_1. This delay is sufficiently long to allow complete relaxation of the system to the ground state, that is, longer than the lifetime of the metastable state, as will be justified later. The final pulse sequence uses the same sequence as P_A, except a microwave π-pulse is applied just before the collection laser pulse in an attempt to invert the populations of $|1\rangle$ and $|2\rangle$, creating the P_B case. As full population inversion was not achieved during the experiment, a factor was implemented in the model to account for the imperfect π-pulse.

For these measurements, the sample was under a fixed external magnetic field of 8 mT and the $m_s = -1$ spin state was used for P_B (i.e., we employed an applied microwave frequency of 3.27 GHz). Each of the three pulse sequences were executed experimentally, using four different relative laser powers (S) ranging from 0.14 to 0.86. The entire set of PL time traces were then globally fit using the 5-level model. The experimental (circles) and calculated (solid line) results are shown in Figure 2c. The same experiment was performed using reflected laser light to demonstrate the shape of the laser pulse and can be viewed in Figure S2, Supporting Information.

The various transition rates in the model were either constrained to reported values or adjusted freely to get the best fit to the experimental PL time trace data. The excited state decay rates ($1/T_{1,|3\rangle}$ and $1/T_{1,|4\rangle}$) have been previously measured to be $1/T_{1,|3\rangle} = k_d + k_{35} = 1.01 \times 10^9$ s^{-1} and $1/T_{1,|4\rangle} = k_d + k_{45} = 2.03 \times 10^9$ s^{-1}, respectively,[28] and so those were fixed in our model. The ratio of k_{51} to k_{52} has been reported as ⅓ for V_B^- defects[28] but was initially left free in our model. The radiative component of the direct decay rate, k_r, has been calculated theoretically to be $k_r = 9.1 \times 10^4$ s^{-1},[37] but no theory is available for the non-radiative component k_{nr}, and so we left the total direct rate $k_d = k_r + k_{nr}$ free in our model. To match the optical excitation rate, we let $k_p = k_{p0} \times S$ where k_{p0} was adjusted freely in the model. Thus, when fitting the model to the experimental data, k_{51}, k_{52}, k_d, and k_{p0} were used as free fit parameters, while k_{35} and k_{45} were set by the value of k_d so as to retain the reported excited state decay rates $1/T_{1,|3\rangle}$ and $1/T_{1,|4\rangle}$. An additional free parameter corresponding to the partial population swap induced by the microwave π-pulse in the third sequence was also included. The population of the $|1\rangle$ state for the unpolarized case was assumed to be ⅓ = 33%. When the best fit to the experimental data was achieved, this population increased (as inferred from the model) to 51% for the P_A condition and then decreased to 36% for the P_B case, as is shown schematically in Figure 2b.

Overall, the 5-level model with the above assumptions and constraints is found to reproduce relatively well the key features seen in the experimental PL traces, as shown in Figure 2c. Notably, after the initial sharp spikes seen in Figure 2c, there are dips in PL intensity at ≈40 ns before the PL increases again to reach an equilibrium. The experimental and modeled data are consistent in this regard for both the unpolarized and P_B cases. The effect can be explained by considering two counteracting processes. The first is rapid trapping of excited electrons in the relatively long-lived metastable state, causing the PL decrease from the initial spike. The second is polarization into the $|1\rangle$ state which causes a (slower) increase in the PL intensity. In the P_A case, the dip remains visible in the experimental data while the model predicts a suppression of this dip. This inconsistency between the modeled and experimental data suggests that the amount of initial spin polarization is overestimated by the model, possibly due to non-spin conserving decay from excited to ground state, or that partial spin depolarization occurs during the 2 μs delay (despite being much shorter than the measured spin lifetime T_1). However, we were not able to reproduce this feature while preserving an overall good fit elsewhere by changing assumptions made within the 5-level model, suggesting that there may be an additional mechanism not captured by this simple model.

Table 1 summarizes the resultant transition rates in the 5-level model. The values of k_{51} and k_{52} found to best fit the entire experimental dataset are $1.3(1) \times 10^7$ s^{-1} and $2.0(1) \times 10^7$ s^{-1}, respectively. The uncertainty values reflect the variations in the fit values observed when changing initial guesses and fit constraints, indicating a relatively robust convergence of the fit. The obtained k_{51} and k_{52} values are in the ratio ≈ ⅗ (½ − ¾ when accounting for uncertainty ranges), which is similar to the reported ⅓ in that k_{51} is lower than k_{52} but not to the same extent. However, using the exact value of ⅓ produced an inadequate fit which can be seen in Figure S3, Supporting Information. The metastable lifetime ($T_{1,|5\rangle}$) is equal to $T_{1,|5\rangle} = 1/(k_{51} + k_{52}) = 30(2)$ ns, which is

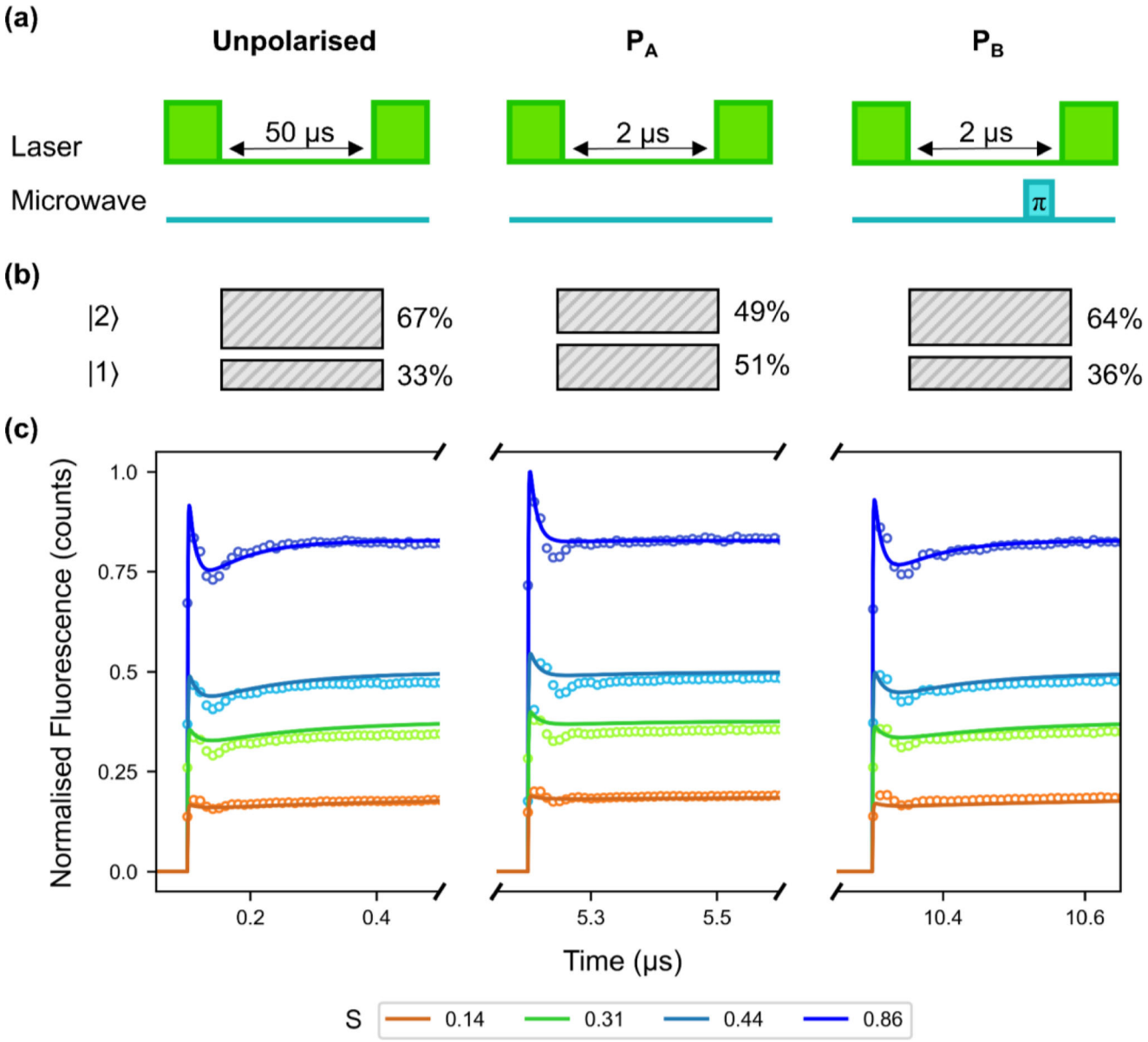

Figure 2. a) Three pulse sequences used to excite the V_B^- from an unpolarized state to primarily $|1\rangle$ polarized (P_A) and primarily $|2\rangle$ polarized (P_B) states. Each laser pulse is 3 µs long. In the third sequence, a microwave π-pulse of 15 ns is applied before the laser pulse to partly polarize the ground state electrons into the $m_s = -1$ spin state (i.e., $|2\rangle$ in our 5-level model). b) Schematic of the ground state electron populations created by the pulse sequences in (a). The values are deduced from the model after fitting shown in (c). c) Time traces of PL intensity from each of the three polarization states measured at four different laser saturation levels (circles). Only the first 500 ns of each laser pulse are shown. Solid lines are a global fit to the data using the 5-level model.

Table 1. Transitions within the V_B^- energy levels and the rates found to best fit experimental data. For the three excited state rates, k_d was used as a fit parameter while k_{35} and k_{45} were set by the relations $k_d + k_{35} = 1.01 \times 10^9\ s^{-1}$ and $k_d + k_{45} = 2.03 \times 10^9\ s^{-1}$. The metastable rates were left as completely free parameters to achieve the best fit to the experimental data. The uncertainty of each value (as shown in brackets) were produced through changing initial guesses for fit values as well as limiting the fit to the first 300 ns to reduce the fitting weight on the PL after reaching equilibrium. A suitable uncertainty range was then chosen to include all viable fit values.

Excited state rates			Metastable state rates	
k_d	k_{35}	k_{45}	k_{51}	k_{52}
$8.8(3) \times 10^8\ s^{-1}$	$1.3(3) \times 10^8\ s^{-1}$	$11.5(3) \times 10^8\ s^{-1}$	$1.3(1) \times 10^7\ s^{-1}$	$2.0(1) \times 10^7\ s^{-1}$

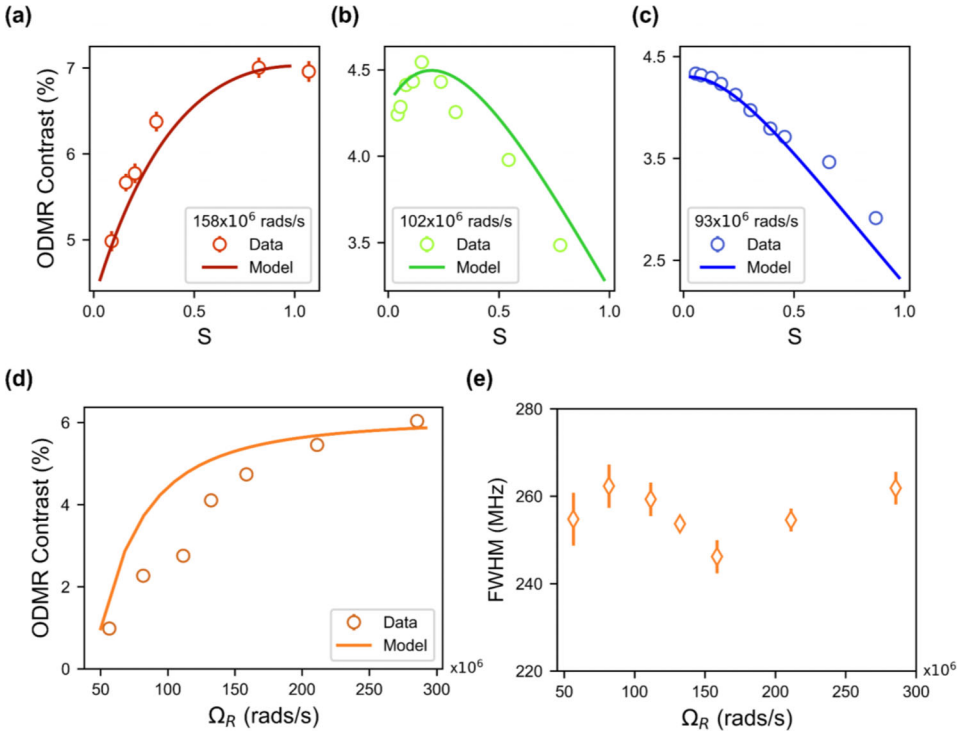

Figure 3. ODMR contrast versus relative laser power (S) at three different Rabi frequencies (Ω_R): a) 158, b) 102, and c) 93 × 10^6 rads s^{-1}, respectively. Both experimental (circles) and simulated (lines) data are shown in the plots. In the model, the microwave driving is entered as a mixing rate k_{MW} with a fixed ratio (adjusted to best fit the data) to the measured Ω_R. d) A plot of experimental and modeled ODMR contrast versus Rabi frequency at $S = 0.16$. e) The change in full width at half maximum (FWHM) of the ODMR measurements over a range of Rabi frequencies. Error bars have been included in all plots, where they are not visible; the size of the marker represents the error.

much shorter than the speculative value proposed previously.[37] We note that such a short metastable lifetime makes a direct measurement of the lifetime through a PL recovery method difficult.[34] The relatively rapid attainment of a steady state of ≈150 ns seen in the experimental PL data in Figure 2c supports the shorter metastable lifetime obtained by our analysis. Meanwhile, the total direct decay rate was found to be $k_d = 8.8(3) \times 10^8$ s^{-1}. This differs greatly from the previously calculated value of the radiative component of $k_r = 9.1 \times 10^4$ s^{-1},[37] indicating the presence of a significant non-radiative decay directly (i.e., bypassing the intersystem crossing) from the excited state to the ground state (k_{nr}). We note that fixing $k_d = k_r = 9.1 \times 10^4$ s^{-1} failed to achieve a good match between the model and experiment (the corresponding attempted fit is shown in Figure S3, Supporting Information).

To further validate the model and the rates displayed in Table 1, we measured the ODMR contrast at various laser and microwave powers and compared the data to predictions made by the model with no additional fit parameter. Due to imperfections in microwave application, such as antenna efficiency, Rabi frequency cannot be directly converted into a rate for the model. As a result, only an approximation of Rabi frequency is feasible which introduces some inconsistencies when fitting to experimental data. In **Figure 3**a–c, the ODMR contrast is plotted against relative laser power (S) at three Rabi frequencies. There are three different trends as Rabi frequency increases. At high frequencies (Figure 3a) ODMR contrast increases with S up to saturation. At low frequencies (Figure 3c), the opposite trend is observed, and intermediate frequencies (Figure 3b) show the transition between these two behaviors (i.e., an increase followed by a decrease in ODMR contrast versus S). This behavior can occur only when the magnitude of k_d is similar to that of k_{35} and k_{45}. Using instead the low theoretical value of $k_d = k_r = 9.1 \times 10^4$ s^{-1} yields an increase in ODMR contrast with S at all Rabi frequencies (see Figure S4, Supporting Information), which is inconsistent with the data.

Figure 3d shows plots of experimental and simulated ODMR contrast versus Ω_R at a laser power of $S = 0.16$. The inconsistency between experimental data and model seen in Figure 3d is attributed to the aforementioned approximation of Rabi frequency used in the model. The model again adequately reproduces the experimental data using the rates listed in Table 1, which further confirms the validity and predictive power of both the model and the obtained transition rates.

Using the rates deduced by the 5-level model, we next studied the dependence of laser and microwave power on magnetic field sensitivity and simulated optimal parameters for sensing using V_B^- centers. The magnetic field sensitivity is calculated using the following equation[22,38]

$$\eta_B \left(T/\sqrt{\text{Hz}}\right) = \mathcal{P}_F \times \frac{1}{\gamma_e} \times \frac{\Delta\nu}{C\sqrt{R}} \quad (1)$$

The electron gyromagnetic ratio (γ_e) is equal to 28 MHz mT^{-1} for V_B^- and $\mathcal{P}_F$ is a numerical parameter that is determined by the spin resonance profile, 0.70 for a Gaussian.[22,38] R is the

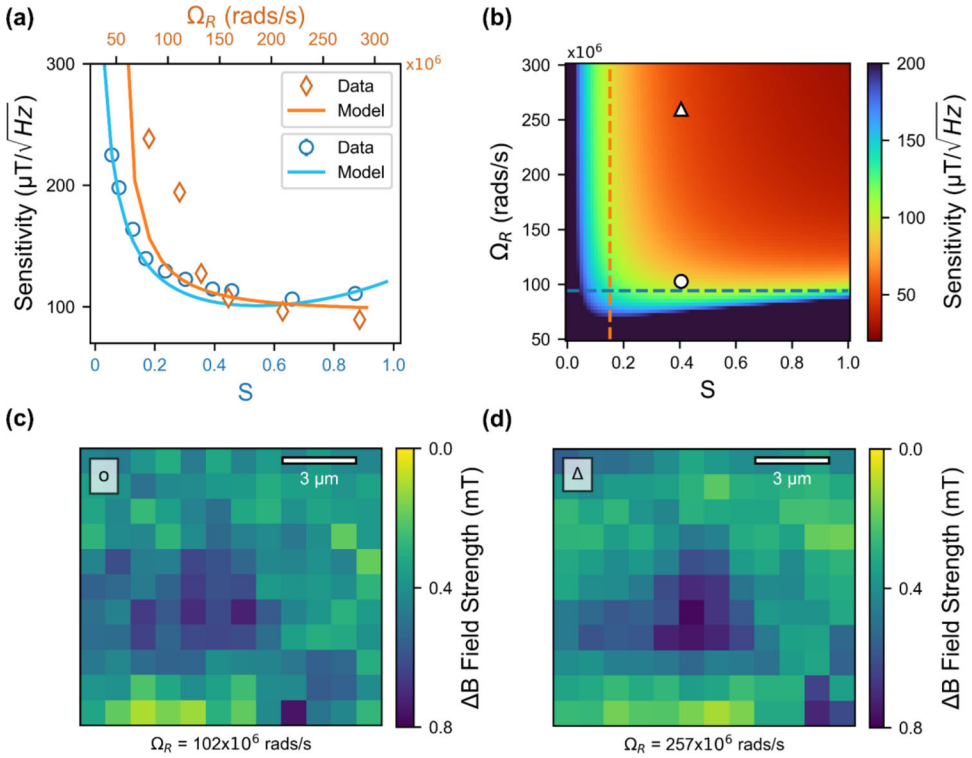

Figure 4. a) Magnetic field sensitivity as a function of relative laser power (circles) and Rabi frequency (diamonds), measured using $\Omega_R = 93 \times 10^6$ rads s^{-1} and $S = 0.16$, respectively. The sensitivity simulated using the 5-level model is also shown on the plot (solid lines). The size of the marker represents the error from the sensitivity calculation. b) A map of sensitivity simulated versus both relative laser power and Rabi frequency. The two dotted lines represent the two measurements from (a). c,d) Magnetic field images of a magnetic particle acquired using the parameters marked in (b) by "o" and "Δ", respectively. These give sensitivity values of 88 and 45 μT $(\sqrt{\text{Hz}})^{-1}$. An optical image of the magnetic particle on top of the hBN flake can be viewed in Figure S5, Supporting Information.

photon count and C is the ODMR contrast. The full width at half maximum (FWHM) of the dips in ODMR spectra ($\Delta\nu$) does not change significantly in our sample across the microwave powers used in this study (Figure 3e). Therefore, a fixed value of 260 MHz is used in sensitivity calculations. For a more detailed discussion, please refer to the Supporting Information.

To obtain the magnetic field sensitivity experimentally, ODMR measurements were performed at various laser and microwaves powers. First, the relative laser power was kept constant at $S = 0.16$, while the microwave power was changed to increase the Rabi frequency from 80×10^6 to 300×10^6 rads s^{-1}. The resulting magnetic field sensitivity is plotted in **Figure 4**a (diamonds). Next, the dependence of magnetic field sensitivity on relative laser power was deduced at a fixed Rabi frequency of 93×10^6 rads s^{-1}. It is also plotted in Figure 4a (circles). In both cases, an increase in laser excitation power or in Rabi frequency improves the magnetic field sensitivity, which reached ≈100 μT $(\sqrt{\text{Hz}})^{-1}$ in our sample. Using the rates found using the 5-level model (Table 1), we calculated the ODMR contrast and photon count rates, and thus simulated the dependencies of sensitivity on relative laser power and Rabi frequency. As is shown by solid lines in Figure 4a, the simulation results are in good agreement with the measured sensitivity data in both cases. The 2D map in Figure 4b shows the sensitivity calculated versus both laser power and Rabi frequency. Dashed horizontal and vertical lines indicate the two conditions where the calculated sensitivity was compared to experimental data in Figure 4a. The map can be used to select optimal parameters for magnetic field sensing. Two sets of conditions, indicated by "o" and "Δ" on the map, were selected to image a magnetic particle on top of an hBN flake. These correspond to a sensitivity of 88 and 45 μT $(\sqrt{\text{Hz}})^{-1}$ at constant relative laser power of $S = 0.45$ and Rabi frequencies of 102×10^6 and 257×10^6 rads s^{-1}, respectively. Figure 4c,d shows magnetic field images obtained under these conditions. To construct these images, ODMR spectra were integrated over 800 microwave frequency sweeps at each pixel and the difference in frequency between the $m_s = 0$ and $m_s = -1$ sublevels was used to deduce the magnetic field strength at each pixel. As predicted by the model, a higher Rabi frequency resulted in better sensitivity and a clearer magnetic field image.

3. Conclusions

In conclusion, we used a 5-level model and time-resolved PL measurements to deduce spin-dependent transition rates in V_B^- defects. The intersystem crossing metastable state lifetime was found to be ≈30 ns, which is much shorter than predicted previously in the literature. The direct decay rate from excited to ground state (potentially non-radiative) was also found to be much larger than predicted, competing with the intersystem

crossing decay pathway. We leveraged these rates to understand and optimize the magnetic sensitivity as a function of laser power and Rabi frequency, and used this optimization to image the field generated by a single magnetic microparticle. Our results are important for future work on quantum sensing and imaging using spin defects in 2D materials.

Supporting Information

Supporting Information is available from the Wiley Online Library or from the author.

Acknowledgements

The authors acknowledge the Australian Research Council (CE200100010, FT220100053, and FT200100073) and the Office of Naval Research Global (N62909-22-1-2028) for the financial support. Dr. John Scott is acknowledged for assistance with ion irradiation.

Open access publishing facilitated by University of Technology Sydney, as part of the Wiley - University of Technology Sydney agreement via the Council of Australian University Librarians.

Conflict of Interest

The authors declare no conflict of interest.

Data Availability Statement

The data that support the findings of this study are available from the corresponding author upon reasonable request.

Keywords

negatively charged boron vacancy, optically detected magnetic resonance, quantum sensing, spin defect

Received: May 3, 2023
Revised: June 22, 2023
Published online: July 14, 2023

[1] P. Maletinsky, S. Hong, M. S. Grinolds, B. Hausmann, M. D. Lukin, R. L. Walsworth, M. Loncar, A. Yacoby, *Nat. Nanotechnol.* **2012**, *7*, 320.
[2] M. Pelliccione, A. Jenkins, P. Ovartchaiyapong, C. Reetz, E. Emmanouilidou, N. Ni, A. C. Bleszynski Jayich, *Nat. Nanotechnol.* **2016**, *11*, 700.
[3] R. W. De Gille, J. M. Mccoey, L. T. Hall, J.-P. Tetienne, E. P. Malkemper, D. A. Keays, L. C. L. Hollenberg, D. A. Simpson, *Proc. Natl. Acad. Sci. USA* **2021**, *118*, e2112749118.
[4] E. V. Levine, M. J. Turner, P. Kehayias, C. A. Hart, N. Langellier, R. Trubko, D. R. Glenn, R. R. Fu, R. L. Walsworth, *Nanophotonics* **2019**, *8*, 1945.
[5] H. L. Stern, Q. Gu, J. Jarman, S. Eizagirre Barker, N. Mendelson, D. Chugh, S. Schott, H. H. Tan, H. Sirringhaus, I. Aharonovich, M. Atatüre, *Nat. Commun.* **2022**, *13*, 618.
[6] A. Gottscholl, M. Diez, V. Soltamov, C. Kasper, A. Sperlich, M. Kianinia, C. Bradac, I. Aharonovich, V. Dyakonov, *Sci. Adv.* **2021**, *7*, eabf3630.
[7] A. Gottscholl, M. Kianinia, V. Soltamov, S. Orlinskii, G. Mamin, C. Bradac, C. Kasper, K. Krambrock, A. Sperlich, M. Toth, I. Aharonovich, V. Dyakonov, *Nat. Mater.* **2020**, *19*, 540.
[8] J.-P. Tetienne, *Nat. Phys.* **2021**, *17*, 1074.
[9] W. Liu, N.-J. Guo, S. Yu, Yu Meng, Z.-P. Li, Y-Ze Yang, Z-An Wang, X.-D. Zeng, L-Ke Xie, Q. Li, J.-F. Wang, J.-S. Xu, Yi-T Wang, J.-S. Tang, C.-F. Li, G.-C. Guo, *Mater. Quantum Technol.* **2022**, *2*, 032002.
[10] A. E. Naclerio, P. R. Kidambi, *Adv. Mater.* **2023**, *35*, 2207374.
[11] X. Gao, S. Pandey, M. Kianinia, J. Ahn, P. Ju, I. Aharonovich, N. Shivaram, T. Li, *ACS Photonics* **2021**, *8*, 994.
[12] X. Xu, A. B. Solanki, D. Sychev, X. Gao, S. Peana, A. S. Baburin, K. Pagadala, Z. O. Martin, S. N. Chowdhury, Y. P. Chen, T. Taniguchi, K. Watanabe, I. A. Rodionov, A. V. Kildishev, T. Li, P. Upadhyaya, A. Boltasseva, V. M. Shalaev, *Nano Lett.* **2023**, *23*, 25.
[13] F. F. Murzakhanov, G. V. Mamin, S. B. Orlinskii, U. Gerstmann, W. G. Schmidt, T. Biktagirov, I. Aharonovich, A. Gottscholl, A. Sperlich, V. Dyakonov, V. A. Soltamov, *Nano Lett.* **2022**, *22*, 2718.
[14] W. Liu, V. Ivády, Z.-P. Li, Y.-Ze Yang, S. Yu, Y. Meng, Z.-A. Wang, N.-J. Guo, F.-F. Yan, Q. Li, J.-F. Wang, J.-S. Xu, X. Liu, Z.-Q. Zhou, Y. Dong, X.-D. Chen, F.-W. Sun, Y.-T. Wang, J.-S. Tang, A. Gali, C.-F. Li, G.-C. Guo, *Nat. Commun.* **2022**, *13*, 5713.
[15] A. J. Healey, S. C. Scholten, T. Yang, J. A. Scott, G. J. Abrahams, I. O. Robertson, X. F. Hou, Y. F. Guo, S. Rahman, Y. Lu, M. Kianinia, I. Aharonovich, J.-P. Tetienne, *Nat. Phys.* **2023**, *19*, 87.
[16] A. Gottscholl, M. Diez, V. Soltamov, C. Kasper, D. Krauße, A. Sperlich, M. Kianinia, C. Bradac, I. Aharonovich, V. Dyakonov, *Nat. Commun.* **2021**, *12*, 4480.
[17] I. O. Robertson, S. C. Scholten, P. Singh, A. J. Healey, F. Meneses, P. Reineck, H. Abe, T. Ohshima, M. Kianinia, I. Aharonovich, J.-P. Tetienne, *arXiv:2302.10560*, **2023**.
[18] X. Gao, S. Vaidya, P. Ju, S. Dikshit, K. Shen, Y. P. Chen, T. Li, *arXiv:2303.02326*, **2023**.
[19] X. Lyu, Q. Tan, L. Wu, C. Zhang, Z. Zhang, Z. Mu, J. Zúñiga-Pérez, H. Cai, W. Gao, *Nano Lett.* **2022**, *22*, 6553.
[20] T. Yang, N. Mendelson, C. Li, A. Gottscholl, J. Scott, M. Kianinia, V. Dyakonov, M. Toth, I. Aharonovich, *Nanoscale* **2022**, *14*, 5239.
[21] M. Huang, J. Zhou, D. Chen, H. Lu, N. J. Mclaughlin, S. Li, M. Alghamdi, D. Djugba, J. Shi, H. Wang, C. R. Du, *Nat. Commun.* **2022**, *13*, 5369.
[22] P. Kumar, F. Fabre, A. Durand, T. Clua-Provost, J. Li, J. H. Edgar, N. Rougemaille, J. Coraux, X. Marie, P. Renucci, C. Robert, I. Robert-Philip, B. Gil, G. Cassabois, A. Finco, V. Jacques, *Phys. Rev. Appl.* **2022**, *18*, L061002.
[23] S. Vaidya, X. Gao, S. Dikshit, I. Aharonovich, T. Li, *arXiv:2302.11169*, **2023**.
[24] W. Liu, Z.-P. Li, Y.-Z. Yang, S. Yu, Y. Meng, Z.-A. Wang, Z.-C. Li, N.-J. Guo, F.-F. Yan, Q. Li, J.-F. Wang, J.-S. Xu, Y.-T. Wang, J.-S. Tang, C.-F. Li, G.-C. Guo, *ACS Photonics* **2021**, *8*, 1889.
[25] M. Hennessey, B. Whitefield, J. A. Scott, M. Kianinia, I. Aharonovich, M. Toth, *arXiv:2303.06784*, **2023**.
[26] N.-J. Guo, W. Liu, Z.-P. Li, Y.-Z. Yang, S. Yu, Y. Meng, Z.-A. Wang, X.-D. Zeng, F.-F. Yan, Q. Li, J.-F. Wang, J.-S. Xu, Y.-T. Wang, J.-S. Tang, C.-F. Li, G.-C. Guo, *ACS Omega* **2022**, *7*, 1733.
[27] A. Sajid, K. S. Thygesen, J. R. Reimers, M. J. Ford, *Commun. Phys.* **2020**, *3*, 153.
[28] S. Baber, R. N. E. Malein, P. Khatri, P. S. Keatley, S. Guo, F. Withers, A. J. Ramsay, I. J. Luxmoore, *Nano Lett.* **2021**, *22*, 461.
[29] Z. Mu, H. Cai, D. Chen, J. Kenny, Z. Jiang, S. Ru, X. Lyu, T. S. Koh, X. Liu, I. Aharonovich, W. Gao, *Phys. Rev. Lett.* **2022**, *128*, 216402.
[30] N. Mathur, A. Mukherjee, X. Gao, J. Luo, B. A. Mccullian, T. Li, A. N. Vamivakas, G. D. Fuchs, *Nat. Commun.* **2022**, *13*, 3233.

[31] P. Yu, H. Sun, M. Wang, T. Zhang, X. Ye, J. Zhou, H. Liu, C.-J. Wang, F. Shi, Y. Wang, J. Du, *Nano Lett.* **2022**, *22*, 3545.
[32] X. Gao, S. Vaidya, K. Li, P. Ju, B. Jiang, Z. Xu, A. E. L. Allcca, K. Shen, T. Taniguchi, K. Watanabe, S. A. Bhave, Y. P. Chen, Y. Ping, T. Li, *Nat. Mater.* **2022**, *21*, 1024.
[33] R. Gong, G. He, X. Gao, P. Ju, Z. Liu, B. Ye, E. A. Henriksen, T. Li, C. Zu, *arXiv:2210.11485*, **2022**.
[34] L. Robledo, H. Bernien, T. V. D. Sar, R. Hanson, *New J. Phys.* **2011**, *13*, 025013.
[35] N. B. Manson, J. P. Harrison, M. J. Sellars, *Phys. Rev. B* **2006**, *74*, 104303.
[36] J.-P. Tetienne, L. Rondin, P. Spinicelli, M. Chipaux, T. Debuisschert, J.-F. Roch, V. Jacques, *New J. Phys.* **2012**, *14*, 103033.
[37] J. R. Reimers, J. Shen, M. Kianinia, C. Bradac, I. Aharonovich, M. J. Ford, P. Piecuch, *Phys. Rev. B* **2020**, *102*, 144105.
[38] X. Gao, B. Jiang, A. E. Llacsahuanga Allcca, K. Shen, M. A. Sadi, A. B. Solanki, P. Ju, Z. Xu, P. Upadhyaya, Y. P. Chen, S. A. Bhave, T. Li, *Nano Lett.* **2021**, *21*, 7708.